

Evidence of an interaction between jets and intra-cluster magnetic layer

James Chibueze (✉ james.chibueze@nwu.ac.za)

North-West University

Haruka Sakemi

Kyushu University

Takumi Ohmura

Kyushu University

Mami Machida

National Astronomical Observatory of Japan

Hiroki Akamatsu

SRON Netherlands Institute for Space Research

Takuya Akahori

National Astronomical Observatory of Japan

Hiroyuki Nakanishi

Kagoshima University

Viral Parekh

South African Radio Astronomy Observatory

Ruby van Rooyen

South African Radio Astronomy Observatory

Tsutomu Takeuchi

Nagoya University, Division of Particle and Astrophysical Science

Physical Sciences - Article

Keywords: Galaxy Clusters, Relativistic Electrons, Intra-cluster Magnetic Fields, Cosmic-ray Re-acceleration

Posted Date: September 23rd, 2020

DOI: <https://doi.org/10.21203/rs.3.rs-81320/v1>

License:   This work is licensed under a Creative Commons Attribution 4.0 International License.

[Read Full License](#)

Version of Record: A version of this preprint was published at Nature on May 5th, 2021. See the published version at <https://doi.org/10.1038/s41586-021-03434-1>.

Evidence of an interaction between jets and intra-cluster magnetic layer

James O. Chibueze^{1,2,†,*}, Haruka Sakemi^{3,‡,*}, Takumi Ohmura^{3,+,*}, Mami Machida⁴, Hiroki Akamatsu⁵, Takuya Akahori⁶, Hiroyuki Nakanishi⁷, Viral Parekh^{8,9}, Ruby van Rooyen⁸, and Tsutomu T. Takeuchi^{10,11}

¹Centre for Space Research, Potchefstroom campus, North-West University, Potchefstroom 2531, South Africa

²Department of Physics and Astronomy, Faculty of Physical Sciences, University of Nigeria, Carver Building, 1 University Road, Nsukka, Nigeria

³Graduated School of Science, Kyushu University, 744 Motooka Nishi-ku, Fukuoka, Fukuoka 819-0395, Japan

⁴Division of Science, National Astronomical Observatory of Japan, 2-21-1 Osawa, Mitaka, Tokyo 181-0015, Japan

⁵SRON Netherlands Institute for Space Research, Sorbonnelaan 2, 3584 CA Utrecht, The Netherlands

⁶Mizusawa VLBI Observatory, National Astronomical Observatory of Japan, 2-21-1 Osawa, Mitaka, Tokyo 181-0015, Japan

⁷Graduate School of Science and Engineering, Kagoshima University, 1-21-35 Korimoto Kagoshima 890-0065, Japan

⁸South African Radio Astronomy Observatory, The Park, Park Road, Pinelands, 2 Fir Street, Black River Park, Observatory, 7925, South Africa

⁹Department of Physics and Electronics, Rhodes University, PO Box 94, Makhanda, 6140, South Africa

¹⁰Division of Particle and Astrophysical Science, Nagoya University, Furo-cho, Chikusa-ku, Nagoya 464-8602, Japan

¹¹The Research Center for Statistical Machine Learning, the Institute of Statistical Mathematics, 10-3 Midori-cho, Tachikawa, Tokyo 190-8562, Japan

†james.chibueze@nwu.ac.za

‡sakemi@phys.kyushu-u.ac.jp

+ohmura@phys.kyushu-u.ac.jp

*Corresponding authors. These authors contributed equally to this work.

Galaxy clusters are known to harbour magnetic field, however, the extent of the influence of the intra-cluster magnetic field on the cluster member galaxies remains an unresolved question. Intra-cluster magnetic field can be observed as density contact discontinuity formed by cool and dense plasma running into hot ambient plasma^{1,2}, and this exist in the central region of a merging galaxy cluster Abell 3376³. Here we report on unambiguous evidence of an interaction between the relativistic electrons and intra-cluster magnetic fields from MeerKAT^{4,5} observations of a radio galaxy MRC 0600-399, having bent jets. Contrary to typical bent jets^{6,7}, the jet shows a 90° bend at the contact discontinuity and the collimated jet further extends over 100 kpc from the bend point. The spectral index flattens downstream of the bend point, indicating cosmic-ray re-acceleration. High-resolution numerical simulations reveal that the ordered magnetic field along the discontinuity, at which the intra-cluster magnetic field can be compressed and amplified, plays a significant role to the change in the direction of the jet propagation. The overall morphology of the bent jet bears remarkable similarities with the simulations, which greatly strengthens our understanding of the interaction between relativistic electrons and intra-cluster magnetic field.

Galaxy clusters, which consist of galaxies, hot, tenuous, and magnetized plasma (intra-cluster medium: ICM), and dark matter, are the largest celestial objects in the Universe^{8,9}. In hierarchical structure formation, the growth of galaxy clusters results in accretion and the merger of sub-halos, this leads to

31 shock waves which heat up the plasma, disturb its motion, and accelerate cosmic-rays¹⁰. Shock waves in
 32 the ICM are also formed by active galactic nucleus (AGN) jets from radio galaxies in clusters. Thus, galaxy
 33 clusters are an ideal celestial laboratory to study plasma physics, an example of which is wide-angle tail
 34 (WAT) radio galaxies^{6,7}. WAT sources commonly exhibit (i) diffuse plume-like structure at the terminal
 35 point of the jet, and (ii) jet bending following the motion of the source. Another example is the so-called
 36 cold front, a density contact discontinuity of the ICM^{1,2}. A cold front is formed by cooled and dense gas
 37 moving in a hotter ambient gas¹¹. Such a motion naturally strips the gas by ram pressure¹² and damps
 38 or amplifies magnetic fields¹³. Since their discovery, WAT sources and cold fronts have been the focus
 39 of many studies to understand their origins, interaction with the ICM, and the nature of the intra-cluster
 40 magnetic field^{12,14–16}. Recently, NGC 4869 in the coma group observed by GMRT was reported as a
 41 possible jet-cold front interaction because it shows a correlation with X-ray intensity and a flat spectral
 42 index after a sharp bent of 70°¹⁷. However, they did not point out the importance of magnetic fields to
 43 form the bent jet.

44 Abell 3376 (Hereafter A3376) is a late-phase violent merging cluster showing a Mpc-scale elongated
 45 X-ray morphology in the east-west direction with a comet-like structure in the central region. Previous
 46 X-ray studies³ revealed the presence of a cold front in front of the 2nd brightest cluster galaxy MRC
 47 0600-399¹⁸ and the presence of shock structures at the outskirts of the cluster. Weak lensing observations
 48 have revealed the presence of two massive sub-clusters in the eastern and western parts of the cluster
 49 and support that this is a high-mass ratio merger ($M_W/M_E = 3.3_{-3.0}^{+2.0}$)¹⁹. However, the observed mass
 50 ratio may be lower than the actual mass ratio because numerical simulations suggested that A3376 has a
 51 mass-ratio of 1:10²⁰. Previous radio observations^{21,22} detected the bent radio jets from MRC 0600-399.
 52 Contrary to the typical WAT sources, the jets bend in the same direction with respect to the sub-cluster’s
 53 motion. In other words, the jets propagate against the ram pressure. Due to the limited angular resolution
 54 in the previous observations, the origin of this unique structure remains a mystery. Combining our radio
 55 interferometric observations with X-ray observations and numerical simulations, we unveiled detailed
 56 structure and formation mechanism of MRC 0600-399.

57 MRC 0600-399 was observed at the center frequency of 1.28 GHz with MeerKAT to investigate the
 58 detailed morphology. Fig. 1 shows the MeerKAT image of 200 kpc radius around the central region
 59 of A3376. There are two prominent radio galaxies - MRC 0600-399 and galaxy B. The magenta-cross
 60 indicates the position of an optical source associated with MRC 0600-399, which is the 2nd brightest
 61 cluster galaxy of A3376¹⁸. The yellow-diamond indicates another optical source associated with galaxy
 62 B which is a D-type elliptical member galaxy of A3376. Galaxy B shows a two-sided jet that is gently
 63 bent and the terminal region of the southern jet has a plume-like structure, implying that galaxy B is a
 64 WAT source. The detailed structures of galaxy B are identified for the first time with the high-dynamic
 65 range observation with MeerKAT. MRC 0600-399 also shows two-sided bent jets, but the collimated
 66 structures continue to the east direction over ~ 100 kpc and ~ 50 kpc for the northern and southern jets,
 67 respectively, beyond the bend points. The bend points refer to the locations (north and south of MRC
 68 0600-399) where the direction of the jet bends 90° to the east as indicated with red dashed circles in Fig. 1.
 69 The radio fluxes of the jets (especially the northern jet) drastically decreases before the bend points. There
 70 are also diffuse faint structures in the opposite (west) direction to the bent jets. We will refer to these as
 71 the “double-scythe”. Moreover, at the southern boundary of the northern bent jet, some diffuse filaments
 72 are resolved for the first time. These filaments appear faint compared to the rest of the emission, but are
 73 detected at well above the noise and indicated real structure related to the northern jet. These features are
 74 very unusual for typical WAT sources. We confirmed that there is no other radio galaxy overlapping with
 75 MRC 0600-399 and causing the “double-scythe” structure, thus, its certainly associated with jets of MRC
 76 0600-399.

77 To understand the nature of MRC 0600-399, we made a spectral index map from the MeerKAT data
78 (Fig. 2 A). The frequency range is from 909 MHz to 1658 MHz, and spectral indices are calculated only
79 for the pixels at which the intensities are higher than 3 times of total intensity root-mean-square (rms)
80 noise levels at all frequencies. We derived the detailed spectral structures of MRC 0600-399. Fig. 2 (B)
81 show one dimensional profiles of the spectral index and flux density along the bent jets. We divided the
82 northern jet into three parts (N1, N2, and N3), and the southern jet into two parts (S1 and S2) based on
83 their properties. The spectral index values gradually decrease in N1 and S1 starting from MRC 0600-399.
84 The spectral index decrement across 49 kpc (7 open circles) is ~ 0.76 for N1, and across 25 kpc (4 open
85 circles) is ~ 0.44 for S1. The trend then drastically changes and these values become fairly constant in N2
86 and S2, suggesting re-acceleration of relativistic electrons. Finally, these values again decrease in N3 with
87 the decrement of ~ 0.69 across 30 kpc (6 open circles). The flux density values show a similar trend with
88 the spectral indices in each part. The flux densities of the radio emission of the jets gradually decreases,
89 and in the bend regions, the flux densities increase clearly. It implies an interaction with surrounding
90 medium around the bend points.

91 Fig. 3 (A) shows the X-ray emission from the ICM with MeerKAT radio emission overlaid on it as
92 contours. Across the northern bent jet (N2 and N3), the X-ray surface brightness gets dimmer. The radial
93 surface brightness profile across the northern bent jet (Fig. 3 A insert) suggests a clear discontinuity, which
94 we interpret as a cold front. Intriguingly, radio emission shows a peak just outside the cold front, where the
95 X-ray surface brightness slightly deviate from the expected values. This is an indication of the presence of
96 a plasma depletion layer due to intra-cluster magnetic field²³. From earlier numerical simulations²⁴⁻²⁶,
97 thick magnetic-field layers around cold fronts can be formed. Indeed, some observational evidence of
98 amplified magnetic field across cold fronts has been reported^{2,27}. All observational evidence and previous
99 numerical simulations point toward an interaction between jets and intra-cluster magnetic field along
100 the cold front. This unusual radio morphology is ascribed to (partly re-accelerated) relativistic electrons
101 traveling along the magnetic fields of jets and the ICM over 150 kpc.

102 In order to understand the jet bending quantitatively, we performed three-dimensional magneto-
103 hydrodynamic (MHD) simulations of the interaction between the jet and the intra-cluster magnetic field
104 using the CANS+ code²⁸. We adopted an arch-shape magnetic field to reproduce the magnetic layer of
105 the cold fronts. A jet launched from MRC 0600-399 travels straight with supersonic speed and hits the
106 magnetic arch. After that, the motion of the jet across the arch is suppressed due to the arch's magnetic
107 tension, and the flow escapes along with the magnetic arch particularly toward the east direction because
108 the tension against the flow is weaker due to the field inclination with respect to the jet injection direction;
109 see Fig. 3 (B) at the elapsed time of 68 Myr from the time of interaction of the jet with the magnetic
110 arch. The escaped flow has a sharp "double-scythe" shape because the Kelvin-Helmholtz instability is
111 suppressed by the strong arch magnetic-fields. The strong fields also produce a backflow of the jet. The
112 backflow collides with the incoming jet and reduce its momentum, resulting in turbulence. As a result, the
113 jet width reaches ten times the initial size around the bend point.

114 The synchrotron radio image made with our simulation data successfully reproduce major characteristic
115 features of the northern jet (Fig.3 C). Firstly, at the bent point, the simulation shows a "double-scythe"
116 shape. Particularly, the eastern emission, which is produced by the majority of the escaped flow, have a
117 close resemblance to the MeerKAT image, while the emission at the western area is more diffuse because
118 of the presence of less gas along this direction. Secondly, the location of radio emission relative to the
119 X-ray profile is qualitatively consistent with the observed one (see Fig. 3 C insert). Thirdly, the simulation
120 reproduces the profile of the radio flux across N1 to N2. As for the southern jet, there are a handful of
121 consistencies such as the "double-scythe" structure and an enhancement of radio flux at the bend point,
122 suggesting the existence of another cold front and the interaction between the jet and ordered magnetic

123 fields. Meanwhile, the simulation shows a more smoothed arc-like structure at the tip of the jet. This
124 difference could be due to the projection effect for a different viewing angle of the jet and/or more complex
125 structure of magnetic fields which is not considered in our simple setup.

126 Our MHD simulation reproduced a 50 kpc long eastern scythe of the northern jet, while the observed
127 emission extends up to 100 kpc from the bend point. This difference suggests that there may be some
128 aspects of the plasma which are not considered in our simulations. One notable non-ideal MHD effect
129 is thermal conduction. Although we do not know an actual thermal conductivity for the ICM, 10% of
130 Spitzer thermal conduction value²⁹ introduces a heat transfer up to ~ 70 kpc for 70 Myr. Diffusion of
131 charged particles across magnetic field tends to be suppressed and the conduction could effectively work
132 for the direction along the ordered magnetic field, which is expected to lie along the cold front due to
133 compression and stretch^{25,26,30}. Such anisotropic propagation of charged particles qualitatively explains
134 the collimated structure. Another possibility is the decoupling between cosmic-rays and thermal plasma.
135 Assuming that the cosmic-ray streaming velocity is of the order of the Alfvén velocity, they move with a
136 speed of 1000 – 5000 km/s for several tens of μG . This speed is 2 – 10 times faster than the speed of the
137 jet flow along the cold front. The synchrotron cooling time of the relativistic electrons responsible for
138 1 GHz radio emission is ~ 6 Myr for 50 μG for instance. The corresponding propagation distance is 30
139 – 50 kpc, broadly consistent with the scythe size from the magnetic reconnection layer where the large
140 current density exists (Fig. 3 D). Relativistic electrons are bounded by the ordered magnetic field along
141 the cold front, so that they naturally explain the collimated structure along the field.

142 Our simulations indicate that the current sheet is generated at the contact area between the jet and
143 magnetic field layer (Fig. 3 D) once the jet collides with the cold front. This suggests that magnetic energy
144 can be efficiently converted to the energy of cosmic-rays at N2 via magnetic reconnection and in-situ
145 particle (re-)acceleration should occur there. Actually, the decrement of the spectral index, i.e. aging of
146 relativistic electrons, halts at N2 (Fig. 2 B). Then, the spectral index and radio flux decrease again at N3.
147 It is likely that we are observing active transportation of the cosmic-ray particles which were generated
148 and/or re-accelerated by magnetic reconnection through the ordered magnetic field in the cold front.

149 Finally, we summarize our new findings in Fig. 4. We report the bending of the jets of MRC 0600-399
150 due to their interactions with compressed intra-cluster magnetic field (cold front). The “double-scythe”
151 structures are formed by the relativistic electrons, both the physical plasma flows and the re-accelerated
152 particles by magnetic reconnection. Our results highlight the role of intra-cluster magnetic field in the
153 evolution of radio galaxies in the clusters. In the near future, wide-field observations of LOFAR, ASKAP,
154 MeerKAT and SKA are expected to provide various evidence of the interaction between jets and the
155 intra-cluster magnetic field, similar to the case of MRC 0600-399 reported in this Letter. These results
156 will allow us discuss the magnetic energy stored in galaxy clusters, the coherent length of the magnetic
157 field, thermal conduction, re-acceleration and transport process of cosmic particles. This means that the
158 “double-scythe jets” become an ideal celestial laboratory to study plasma physics.

159 **Methods**

160 We assume that Hubble’s constant $H_0 = 70 \text{ km s}^{-1} \text{ Mpc}^{-1}$, the density parameter for mass $\Omega_M = 0.27$
161 and for dark energy $\Omega_\Lambda = 0.73$, which gives 54.5 kpc/arcmin at $z = 0.046$. Unless otherwise stated, the
162 errors correspond to 68% confidence for each parameter.

163 **MeerKAT L-band observations and data reduction**

164 Abell 3376 East was observed with 60 antennas of the MeerKAT array^{4,5} on 1 June, 2019 (Project ID:
165 SCI-20190418-JC-01) at L-band (856 MHz to 1712 MHz). The MeerKAT array, located in the Northern

166 Karoo desert of South Africa, is made up of 64 13.5-m “offset Gregorian” parabolic dish antennas. 48 of
167 the 64 antennas are located in the inner core (within 1 km radius) providing the shortest baseline of 29 m,
168 while the other 16 antennas are spread outside the core up to a maximum baseline of 8 km. Thus, MeeKAT
169 is capable of recovering a wide range ($5''$ to $27'$) of angular scales at the central frequency of 1283 MHz.

170 The primary flux and bandpass calibrator was fixed to J0408-6545 (the total intensity, $I = 17$ Jy at
171 1283 MHz). J0616-3456 ($I = 3.1$ Jy at 1283 MHz, and 5.7° from the phase tracking center of Abell 3376
172 East) was used as the secondary gain calibrator. During the observations, we performed four 10-minute
173 scans of the primary calibrator, we scanned the secondary calibrator for every two minutes after the scan
174 of the target. The flux, bandpass, and gain calibrations were reliably done with these bright calibrators.

175 The data correlation was done with the SKARAB correlator³¹ in 4k mode with 856 MHz bandwidth,
176 4096 channels of ~ 209 kHz per channel. Then, we have reduced the data with the semi-automated
177 MeerKAT data analysis pipelines - OXKAT¹.

178 OXKAT is a semi-automatic pipeline (developed by Ian Heywood) used for MeerKAT data reduction
179 and employs a collection of publicly available radio interferometry data flagging, calibration and imaging
180 software packages. In the flagging process, the known radio frequency interference (RFI) channels,
181 856 MHz to 880 MHz, 1658 MHz to 1800 MHz, and 1419.8 MHz to 1421.3 MHz, are unexceptionally
182 flagged out. Then, other possible RFIs are flagged using the autoflagger tricolour for the calibrators and by
183 using AOFlagger³² for the target fields. OXKAT pipeline uses the customary tasks from the CASA³³ suite
184 for cross-calibration.

185 To deconvolve and image the target data, the WSClean imager³⁴ with Briggs weighting and a robust
186 parameter of -0.3 was used, with the multi-scale and wide-band deconvolution algorithms enabled to
187 better allow imaging diffuse emission present in the our fields. Deconvolution was performed in ten
188 sub-band images of each 107 MHz wide-band. WSClean generates the multi-frequency synthesis (MFS)
189 map (full bandwidth map), in joined-channel deconvolution mode, has central frequency of 1283 MHz.
190 OXKAT pipeline uses the customary tasks from the Cubical software³⁵ for self-calibration.

191 We achieved synthesized beam of $5''.8 \times 5''.5$ and the rms noise level is $4.2 \mu\text{Jy beam}^{-1}$ in the MFS
192 image. The center frequency of the sub-band images are 909, 1016, 1123, 1230, 1337, 1444, 1551, and
193 1658 MHz. To derive the spectral index map (Fig. 2 B), we smoothed the resolutions of the sub-band
194 images to the resolution ($9''.5 \times 8''.5$) of 909 MHz sub-band image using CASA "imsmooth" task.

195 **XMM-Newton observation and Surface brightness profile analysis**

196 The radio galaxy was observed with EPIC instruments on the XMM-Newton X-ray observatory at 2003
197 (OBSID: 0151900101). The data was reduced with the science analysis system (SAS) and extended
198 source analysis software (ESAS) packages, following the processing described in³. The tools emchain and
199 epchain were used to create the reduced EPIC-MOS and pn event files, respectively. Light curves were
200 extracted with 100s bins and screened for background flares with mos-filter and pn-filter. The cleaned
201 exposure time for two MOS and pn data are 18.5 ks and 18.5 ks, respectively. The events with PATTERN
202 values greater than 12 (MOS)/4 (pn) and non-zero FLAG values were excluded. The point sources with
203 flux $> 4 \times 10^{-14}$ erg/s/cm² were excluded from the image. The resultant 0.5–2.0 keV X-ray image was
204 shown in Fig. 3 (A).

To investigate correlation with the bended radio emission, we fit the X-ray surface brightness profile

¹<https://ascl.net/code/v/2627>

with `Proffitt`³⁶. To model the observed profile, we used an underlying broken power-law density model:

$$n(r) = \begin{cases} Cn_0 \left(\frac{r}{r_{\text{edge}}} \right)^{-\alpha_1}, & r \leq r_{\text{edge}} \\ n_0 \left(\frac{r}{r_{\text{edge}}} \right)^{-\alpha_2}, & r > r_{\text{edge}}. \end{cases} \quad (1)$$

where α , r_{edge} , n_0 and C represent the slope of the profile, the location of the density jump, the normalization constant and compression factor (density ratio), respectively. The subscripts 1, 2 denote inside and outside of the edge of the density jump. The density model profile is projected into the line of sight assuming spherical geometry within the extraction sector.

We fit the surface brightness profile in the annular shown in Fig. 3 (A). The opening angles 60° – 120° centered on (6:02:13.014, -39:56:56.58) were selected to cover the bended jet structure. The extracted surface brightness profile was radially binned to obtain $\text{SNR} > 7$. The observed profile was well reproduced with above model with $\chi^2 = 93.2$ for 83 d.o.f ($\Delta\chi = 1.1$). The observed and the best-fitted model profiles are shown in Fig. 3 (A) insert. We find a surface brightness break across the region where the jet bends almost 90° . The resultant density jump ($C = 1.6 \pm 0.1$) is comparable to the previous report on the tip of the sub-cluster ($C = 1.8 \pm 0.2$ ³). Since the presence of the cold front was confirmed at the tip of the sub-cluster, it is natural to consider the observed density jump is an extension of the cold front.

Numerical Simulation

A cold front is just a contact discontinuity and hence it has been thought that it does not significantly affect the jet dynamics. Thus, few studies have focused on the interaction between jets and a cold front. Meanwhile, the results of both X-ray observations and magnetohydrodynamic (MHD) simulation suggest ordered magnetic fields, whose strength can be a several tens of μG , near the front. If the energy of ordered fields are comparable the kinetic energy of radio jets, the jets should be bent by the Maxwell stress. In this paper, we focus mainly on the jet bending process by jet-cold front interaction. The original idea of bending jet by misaligned magnetic field was proposed by Koide and collaborators³⁷.

To study the interaction between jet and a magnetic layer behind cold front, we have conducted three dimensional MHD simulations using CANS+ code²⁸. The units of length, velocity, density, pressure, temperature, and time in our simulations are $r_0 = 2 \text{ kpc}$, $v_0 = 1000 \text{ km s}^{-1}$, $\rho_0 = 5 \times 10^{-27} \text{ cm}^{-3}$, $p_0 = 3 \times 10^{-11} \text{ erg cm}^{-3}$, $kT_0 = 4 \text{ keV}$, and $t_0 = 2.4 \text{ Myr}$ respectively. We use the Cartesian domain $(-78r_0, 78r_0) \times (0, 96r_0) \times (-31.5r_0, 31.5r_0)$ and uniform grids, whose size is $\Delta x = \Delta y = \Delta z = 0.15 r_0$. Here, the y direction is aligned with jet axis. We impose a zero-gradient boundaries on all the sides of the box.

To mimic a magnetic layer of a cold front, we set a magnetic arch as follow:

$$B_\theta(r) = B_0 + B_1 \sin \{(r - r_s)\pi/w\}, \quad B_r = B_z = 0, \quad (2)$$

where $r = \sqrt{x^2 + y^2}$, $B_0 = 3 \mu\text{G}$, $B_1 = 60 \mu\text{G}$, $r_s = 55r_0$, $w = 15r_0$, respectively. ICM have a constant density, $\rho_{\text{ICM}} = \rho_0$, and ICM pressure profile is determined by the equilibrium condition:

$$p(r) = p(r=0) - \frac{B_\theta^2(r)}{8\pi} - \int_0^r \frac{B_\theta^2(r)}{4\pi r} dr, \quad (3)$$

where $p(r=0) = 5p_0$.

The jet is injected at $(x, y, z) = (30r_0, 0, 0)$, with a radius, $r_{\text{jet}} = 1.5r_0$. The density, pressure, and velocity of injected flow are $\rho_{\text{jet}} = 0.01\rho_0$, $p_{\text{jet}} = 5p_0$, and $v_{y,\text{jet}} = 1.5\sqrt{\gamma p_{\text{jet}}/\rho_{\text{jet}}}$, respectively. Therefore,

234 the jet thermal and kinetic energies are about 3.7×10^{44} erg s⁻¹ and 6.8×10^{44} erg s⁻¹, respectively. Jet
 235 injection continues during simulation time.

236 We use a passive tracer function, $f(x, y, z, t)$, which is injected with the jet to divide it from that of the
 237 ICM. The tracer function have initially zero value elsewhere. To clarify the distribution of jet plasma after
 238 the interaction, the tracer function takes the values of 1.0 in the injected region after 100 Myr.

We model the radio by integrating the emissivity along the line of sight. The synchrotron emissivity, dropping physical constants, are then give by³⁸

$$\varepsilon_{\text{sy}} = NB_{\perp}^{\frac{1}{2}(\alpha+1)}, \quad (4)$$

239 where $N, B_{\perp}, \alpha = 0.5$ is the number density of relativistic electrons and the magnetic field perpendicular
 240 to the projection of the sky, and the power-law synchrotron spectral index, respectively. We model the
 241 population of relativistic electrons via the factor fp . Thus, we do not take into account for energy gain or
 242 loss processes and transportation process, such as diffusion and/or streaming.

We also calculate X-ray surface brightness to investigate correlation between radio jets and a location of cold front. Although the 0.5 - 2.0 KeV X-ray emissivity is roughly proportional to n_e^2 , we set a uniform ICM in our simulation. Therefore, we factorize the density as $n_e = n_{e,\text{background}} \times (\rho/\rho_0)^{39}$. Here, $n_{e,\text{background}}$ is the background density profile, and we adopt the β -model:

$$n_{e,\text{background}}(r) = \begin{cases} Cn_0 \{1 + (r/r_c)\}^{-3\beta/2}, & r \leq r_{\text{edge}} \\ n_0 \{1 + (r/r_c)\}^{-3\beta/2}, & r > r_{\text{edge}}, \end{cases} \quad (5)$$

243 where $r = \sqrt{x^2 + y^2 + z^2}$, $C = 1.6, n_0 = 10^{-3}$ cm⁻³, $r_c = 25$ kpc, $r_{\text{edge}} = 110$ kpc, respectively. r_{edge} is
 244 the location of cold front assuming that the edge of magnetic layer.

245 References

- 246 1. Markevitch, M. *et al.* Chandra Observation of Abell 2142: Survival of Dense Subcluster Cores in a
 247 Merger. **541**, 542–549, DOI: [10.1086/309470](https://doi.org/10.1086/309470) (2000). [astro-ph/0001269](https://arxiv.org/abs/astro-ph/0001269).
- 248 2. Vikhlinin, A., Markevitch, M. & Murray, S. S. A Moving Cold Front in the Intergalactic Medium of
 249 A3667. **551**, 160–171, DOI: [10.1086/320078](https://doi.org/10.1086/320078) (2001). [astro-ph/0008496](https://arxiv.org/abs/astro-ph/0008496).
- 250 3. Urdampilleta, I. *et al.* X-ray study of the double radio relic Abell 3376 with Suzaku. **618**, A74, DOI:
 251 [10.1051/0004-6361/201732496](https://doi.org/10.1051/0004-6361/201732496) (2018). [1806.07817](https://arxiv.org/abs/1806.07817).
- 252 4. Jonas, J. & MeerKAT Team. The MeerKAT Radio Telescope. In *MeerKAT Science: On the Pathway*
 253 *to the SKA*, 1 (2016).
- 254 5. Mauch, T. *et al.* The 1.28 GHz MeerKAT DEEP2 Image. **888**, 61, DOI: [10.3847/1538-4357/ab5d2d](https://doi.org/10.3847/1538-4357/ab5d2d)
 255 (2020). [1912.06212](https://arxiv.org/abs/1912.06212).
- 256 6. Owen, F. N. & Rudnick, L. Radio sources with wide-angle tails in Abell clusters of galaxies. **205**,
 257 L1–L4, DOI: [10.1086/182077](https://doi.org/10.1086/182077) (1976).
- 258 7. Jones, T. W. & Owen, F. N. Hot gas in elliptical galaxies and the formation of head-tail radio sources.
 259 **234**, 818–824, DOI: [10.1086/157561](https://doi.org/10.1086/157561) (1979).
- 260 8. Sarazin, C. L. X-ray emission from clusters of galaxies. *Rev. Mod. Phys.* **58**, 1–115, DOI: [10.1103/](https://doi.org/10.1103/RevModPhys.58.1)
 261 [RevModPhys.58.1](https://arxiv.org/abs/RevModPhys.58.1) (1986).

- 262 9. Carilli, C. L. & Taylor, G. B. Cluster Magnetic Fields. **40**, 319–348, DOI: [10.1146/annurev.astro.40.](https://doi.org/10.1146/annurev.astro.40.060401.093852)
263 [060401.093852](https://doi.org/10.1146/annurev.astro.40.060401.093852) (2002). [astro-ph/0110655](https://arxiv.org/abs/astro-ph/0110655).
- 264 10. Markevitch, M. & Vikhlinin, A. Shocks and cold fronts in galaxy clusters. **443**, 1–53, DOI:
265 [10.1016/j.physrep.2007.01.001](https://doi.org/10.1016/j.physrep.2007.01.001) (2007). [astro-ph/0701821](https://arxiv.org/abs/astro-ph/0701821).
- 266 11. Zuhone, J. A. & Roediger, E. Cold fronts: probes of plasma astrophysics in galaxy clusters. *J. Plasma*
267 *Phys.* **82**, 535820301, DOI: [10.1017/S0022377816000544](https://doi.org/10.1017/S0022377816000544) (2016). [1603.08882](https://arxiv.org/abs/1603.08882).
- 268 12. Gunn, J. E. & Gott, I., J. Richard. On the Infall of Matter Into Clusters of Galaxies and Some Effects
269 on Their Evolution. **176**, 1, DOI: [10.1086/151605](https://doi.org/10.1086/151605) (1972).
- 270 13. Donnert, J., Vazza, F., Brüggem, M. & ZuHone, J. Magnetic Field Amplification in Galaxy Clusters
271 and Its Simulation. **214**, 122, DOI: [10.1007/s11214-018-0556-8](https://doi.org/10.1007/s11214-018-0556-8) (2018). [1810.09783](https://arxiv.org/abs/1810.09783).
- 272 14. Werner, N. *et al.* Deep Chandra observation and numerical studies of the nearest cluster cold front in
273 the sky. **455**, 846–858, DOI: [10.1093/mnras/stv2358](https://doi.org/10.1093/mnras/stv2358) (2016). [1506.06429](https://arxiv.org/abs/1506.06429).
- 274 15. Walker, S. A., ZuHone, J., Fabian, A. & Sanders, J. The split in the ancient cold front in the Perseus
275 cluster. *Nat. Astron.* **2**, 292–296, DOI: [10.1038/s41550-018-0401-8](https://doi.org/10.1038/s41550-018-0401-8) (2018). [1803.00898](https://arxiv.org/abs/1803.00898).
- 276 16. Nolting, C., Jones, T. W., O’Neill, B. J. & Mendygral, P. J. Interactions between Radio Galaxies and
277 Cluster Shocks. I. Jet Axes Aligned with Shock Normals. **876**, 154, DOI: [10.3847/1538-4357/ab16d6](https://doi.org/10.3847/1538-4357/ab16d6)
278 (2019). [1904.05943](https://arxiv.org/abs/1904.05943).
- 279 17. Lal, D. V. NGC 4869 in the Coma cluster: twist, wrap, overlap and bend. *arXiv e-prints*
280 [arXiv:2009.07146](https://arxiv.org/abs/2009.07146) (2020). [2009.07146](https://arxiv.org/abs/2009.07146).
- 281 18. Durret, F. *et al.* The merging cluster of galaxies Abell 3376: an optical view. **560**, A78, DOI:
282 [10.1051/0004-6361/201322082](https://doi.org/10.1051/0004-6361/201322082) (2013). [1310.7493](https://arxiv.org/abs/1310.7493).
- 283 19. Monteiro-Oliveira, R. *et al.* Weak lensing and spectroscopic analysis of the nearby dissociative
284 merging galaxy cluster Abell 3376. **468**, 4566–4578, DOI: [10.1093/mnras/stx791](https://doi.org/10.1093/mnras/stx791) (2017). [1612.07935](https://arxiv.org/abs/1612.07935).
- 285 20. Machado, R. E. G. & Lima Neto, G. B. Simulations of the merging galaxy cluster Abell 3376. **430**,
286 3249–3260, DOI: [10.1093/mnras/stt127](https://doi.org/10.1093/mnras/stt127) (2013). [1301.4434](https://arxiv.org/abs/1301.4434).
- 287 21. Bagchi, J. *et al.* Evidence for shock acceleration and intergalactic magnetic fields in a large-scale
288 filament of galaxies ZwCl 2341.1+0000. **7**, 249–277, DOI: [10.1016/S1384-1076\(02\)00137-9](https://doi.org/10.1016/S1384-1076(02)00137-9) (2002).
289 [astro-ph/0204389](https://arxiv.org/abs/astro-ph/0204389).
- 290 22. Bagchi, J., Durret, F., Neto, G. B. L. & Paul, S. Giant Ringlike Radio Structures Around Galaxy
291 Cluster Abell 3376. *Science* **314**, 791–794, DOI: [10.1126/science.1131189](https://doi.org/10.1126/science.1131189) (2006). [astro-ph/0611297](https://arxiv.org/abs/astro-ph/0611297).
- 292 23. Wang, Q. H. S., Markevitch, M. & Giacintucci, S. The Merging Galaxy Cluster A520—A Broken-up
293 Cool Core, A Dark Subcluster, and an X-Ray Channel. **833**, 99, DOI: [10.3847/1538-4357/833/1/99](https://doi.org/10.3847/1538-4357/833/1/99)
294 (2016). [1603.05232](https://arxiv.org/abs/1603.05232).
- 295 24. Takizawa, M. Hydrodynamic Simulations of a Moving Substructure in a Cluster of Galaxies: Cold
296 Fronts and Turbulence Generation. **629**, 791–796, DOI: [10.1086/431927](https://doi.org/10.1086/431927) (2005). [astro-ph/0505274](https://arxiv.org/abs/astro-ph/0505274).
- 297 25. Asai, N., Fukuda, N. & Matsumoto, R. Three-dimensional Magnetohydrodynamic Simulations
298 of Cold Fronts in Magnetically Turbulent ICM. **663**, 816–823, DOI: [10.1086/518235](https://doi.org/10.1086/518235) (2007).
299 [astro-ph/0703536](https://arxiv.org/abs/astro-ph/0703536).
- 300 26. ZuHone, J. A., Markevitch, M. & Lee, D. Sloshing of the Magnetized Cool Gas in the Cores of
301 Galaxy Clusters. **743**, 16, DOI: [10.1088/0004-637X/743/1/16](https://doi.org/10.1088/0004-637X/743/1/16) (2011). [1108.4427](https://arxiv.org/abs/1108.4427).

- 302 **27.** Chen, H., Jones, C., Andrade-Santos, F., ZuHone, J. A. & Li, Z. Gas Sloshing in Abell 2204: Constraining
303 the Properties of the Magnetized Intracluster Medium. **838**, 38, DOI: [10.3847/1538-4357/aa64de](https://doi.org/10.3847/1538-4357/aa64de)
304 (2017). [1703.01895](https://arxiv.org/abs/1703.01895).
- 305 **28.** Matsumoto, Y. *et al.* Magnetohydrodynamic simulation code CANS+: Assessments and applications.
306 **71**, 83, DOI: [10.1093/pasj/psz064](https://doi.org/10.1093/pasj/psz064) (2019). [1611.01775](https://arxiv.org/abs/1611.01775).
- 307 **29.** Chandran, B. D. G. & Maron, J. L. Thermal Conduction and Particle Transport in Strong Mag-
308 netohydrodynamic Turbulence, with Application to Galaxy Cluster Plasmas. **602**, 170–180, DOI:
309 [10.1086/380897](https://doi.org/10.1086/380897) (2004). [astro-ph/0303214](https://arxiv.org/abs/astro-ph/0303214).
- 310 **30.** Vikhlinin, A., Markevitch, M. & Murray, S. S. Chandra Estimate of the Magnetic Field Strength near
311 the Cold Front in A3667. **549**, L47–L50, DOI: [10.1086/319126](https://doi.org/10.1086/319126) (2001). [astro-ph/0008499](https://arxiv.org/abs/astro-ph/0008499).
- 312 **31.** Hickish, J. *et al.* A Decade of Developing Radio-Astronomy Instrumentation using CASPER Open-
313 Source Technology. *J. Astron. Instrumentation* **5**, 1641001–12, DOI: [10.1142/S2251171716410014](https://doi.org/10.1142/S2251171716410014)
314 (2016). [1611.01826](https://arxiv.org/abs/1611.01826).
- 315 **32.** Offringa, A. R., van de Gronde, J. J. & Roerdink, J. B. T. M. A morphological algorithm for
316 improving radio-frequency interference detection. **539**, A95, DOI: [10.1051/0004-6361/201118497](https://doi.org/10.1051/0004-6361/201118497)
317 (2012). [1201.3364](https://arxiv.org/abs/1201.3364).
- 318 **33.** McMullin, J. P., Waters, B., Schiebel, D., Young, W. & Golap, K. CASA Architecture and Applications.
319 In Shaw, R. A., Hill, F. & Bell, D. J. (eds.) *Astronomical Data Analysis Software and Systems XVI*,
320 vol. 376 of *Astronomical Society of the Pacific Conference Series*, 127 (2007).
- 321 **34.** Offringa, A. R. *et al.* WSCLEAN: an implementation of a fast, generic wide-field imager for radio
322 astronomy. **444**, 606–619, DOI: [10.1093/mnras/stu1368](https://doi.org/10.1093/mnras/stu1368) (2014). [1407.1943](https://arxiv.org/abs/1407.1943).
- 323 **35.** Kenyon, J. S., Smirnov, O. M., Grobler, T. L. & Perkins, S. J. CUBICAL - fast radio interferometric
324 calibration suite exploiting complex optimization. **478**, 2399–2415, DOI: [10.1093/mnras/sty1221](https://doi.org/10.1093/mnras/sty1221)
325 (2018). [1805.03410](https://arxiv.org/abs/1805.03410).
- 326 **36.** Eckert, D. *et al.* The gas distribution in the outer regions of galaxy clusters. **541**, A57, DOI:
327 [10.1051/0004-6361/201118281](https://doi.org/10.1051/0004-6361/201118281) (2012). [1111.0020](https://arxiv.org/abs/1111.0020).
- 328 **37.** Koide, S., Sakai, J.-I., Nishikawa, K.-I. & Mutel, R. L. Numerical Simulation of Bent Jets: Propagation
329 into an Oblique Magnetic Field. **464**, 724, DOI: [10.1086/177359](https://doi.org/10.1086/177359) (1996).
- 330 **38.** Rybicki, G. B. & Lightman, A. P. *Radiative Processes in Astrophysics* (1986).
- 331 **39.** Komarov, S., Reynolds, C. & Churazov, E. Propagation of weak shocks in cool-core galaxy clusters
332 in two-temperature magnetohydrodynamics with anisotropic thermal conduction. **497**, 1434–1442,
333 DOI: [10.1093/mnras/staa1986](https://doi.org/10.1093/mnras/staa1986) (2020). [2004.13252](https://arxiv.org/abs/2004.13252).
- 334 **40.** Joye, W. A. & Mandel, E. New Features of SAOImage DS9. In Payne, H. E., Jedrzejewski, R. I. &
335 Hook, R. N. (eds.) *Astronomical Data Analysis Software and Systems XII*, vol. 295 of *Astronomical*
336 *Society of the Pacific Conference Series*, 489 (2003).
- 337 **41.** Astropy Collaboration *et al.* Astropy: A community Python package for astronomy. **558**, A33, DOI:
338 [10.1051/0004-6361/201322068](https://doi.org/10.1051/0004-6361/201322068) (2013). [1307.6212](https://arxiv.org/abs/1307.6212).

339 Acknowledgements

340 JOC acknowledges support from the Italian Ministry of Foreign Affairs and International Cooperation
341 (MAECI Grant Number ZA18GR02) and the South African Department of Science and Technology's

342 National Research Foundation (DST-NRF Grant Number 113121) as part of the ISARP RADIOSKY2020
343 Joint Research Scheme. VP acknowledges the financial assistance from the South African Radio Astron-
344 omy Observatory (SARAO) and the South African Research Chairs Initiative of the Department of Science
345 and Technology and National Research Foundation. This paper makes use of the MeerKAT data (Project
346 ID: SCI-20190418-JC-01). The MeerKAT telescope is operated by the South African Radio Astronomy
347 Observatory, which is a facility of the National Research Foundation, an agency of the Department of
348 Science and Innovation (DSI). SRON is supported financially by NWO, the Netherlands Organization for
349 Scientific Research. Numerical computations and analyses were partially carried out on Cray XC50 and
350 analysis servers at Center for Computational Astrophysics, National Astronomical Observatory of Japan,
351 respectively. The computation was carried out using the computer resource by Research Institute for Infor-
352 mation Technology, Kyushu University. This work was supported by JSPS KAKENHI Grant Numbers
353 HS: 20J13339, TO: 20J12591, MM: 19K03916, and TTT: 17H01110 and 19H05076. TTT has also been
354 supported in part by the Sumitomo Foundation Fiscal 2018 Grant for Basic Science Research Projects
355 (180923), and the Collaboration Funding of the Institute of Statistical Mathematics “New Development of
356 the Studies on Galaxy Evolution with a Method of Data Science”. SAOImageDS9 development was made
357 possible by funding from the Chandra X-ray Science Center (CXC), the High Energy Astrophysics Science
358 Archive Center (HEASARC) and the JWST Mission office at the Space Telescope Science Institute⁴⁰.
359 This research used of Astropy, a community-developed core Python package for Astronomy⁴¹.

360 **Author contributions statement**

361 J.O.C. conducted the observations and data reduction. V.P. also participated in the MeerKAT data reduction,
362 while H.S. analysed the results and digested their implementations. T.O. and M.M. constructed theory,
363 model and, conducted the numerical simulations. H.A. performed X-ray data analysis. T.A. contributed to
364 writing the MeerKAT proposal and the scientific discussions. T.T.T., R.vR., and H. N. contributed to the
365 scientific discussions. All authors reviewed the manuscript.

366 **Additional information**

367 **Competing interests:** The authors declare no competing interests.

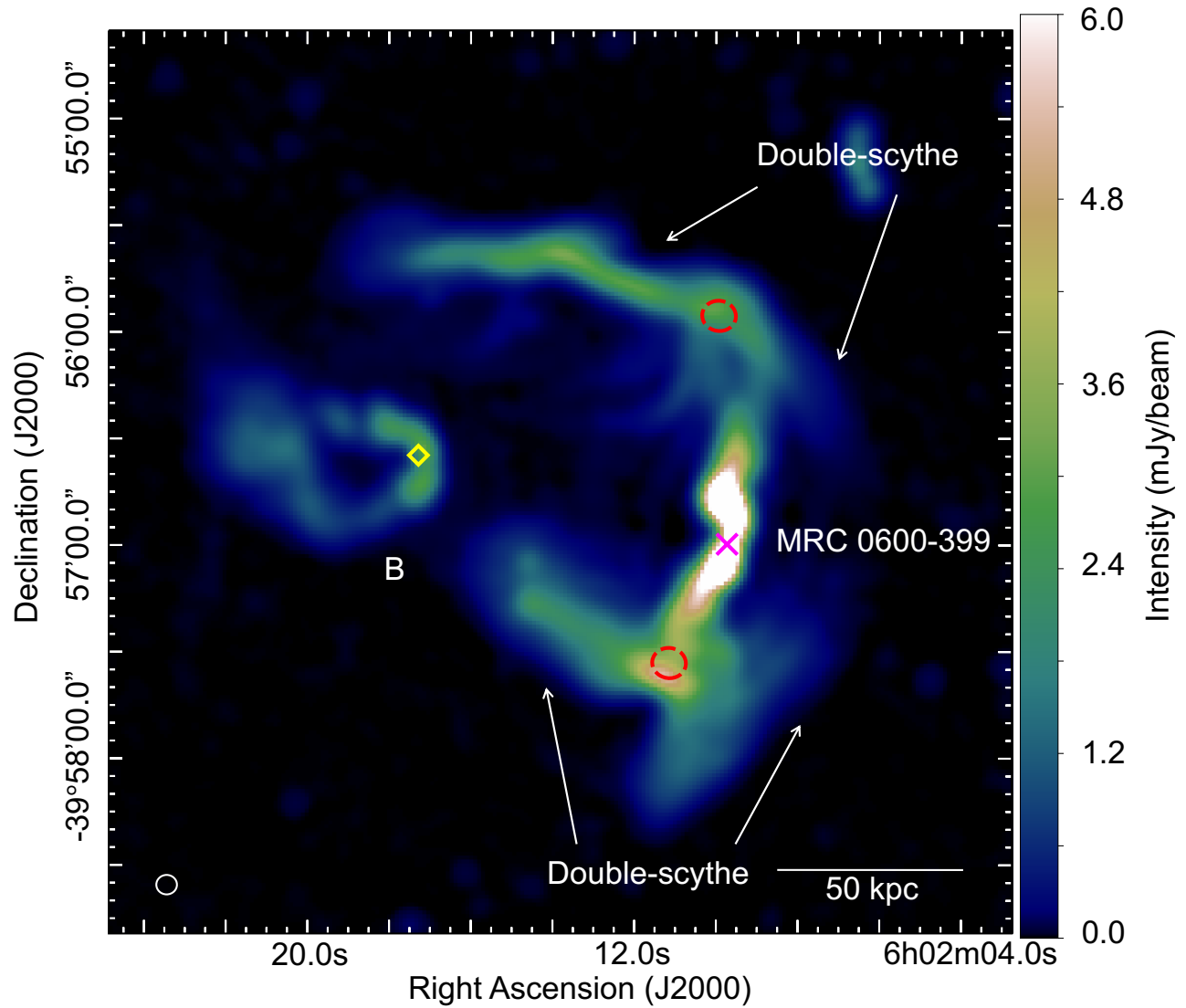


Figure 1. MeerKAT image of the total intensity at the center frequency of 1.28 GHz. The beam size is shown in bottom-left corner, $5.80 \times 5.48 \text{ arcsec}^2$. The magenta cross point indicates the position of the 2nd brightest cluster galaxy in optical band associated with MRC 0600-399. MRC 0600-399 has jets which are bent 90 degree to the east, and continue to the east direction while keeping their collimated shapes. The arrows show the “double-scythe” structures, while the red dashed circles show the bend points. The yellow diamond point shows the position of optical source associated with galaxy B. Galaxy B has also a two-sided jet, but they bend gently and the southern jet has a plume-like structure at the tail. We determined the distance and the length of the scale bar on the basis of the values of the Hubble’s constant = $70 \text{ km s}^{-1} \text{ Mpc}^{-1}$ and the redshift $z=0.046$.

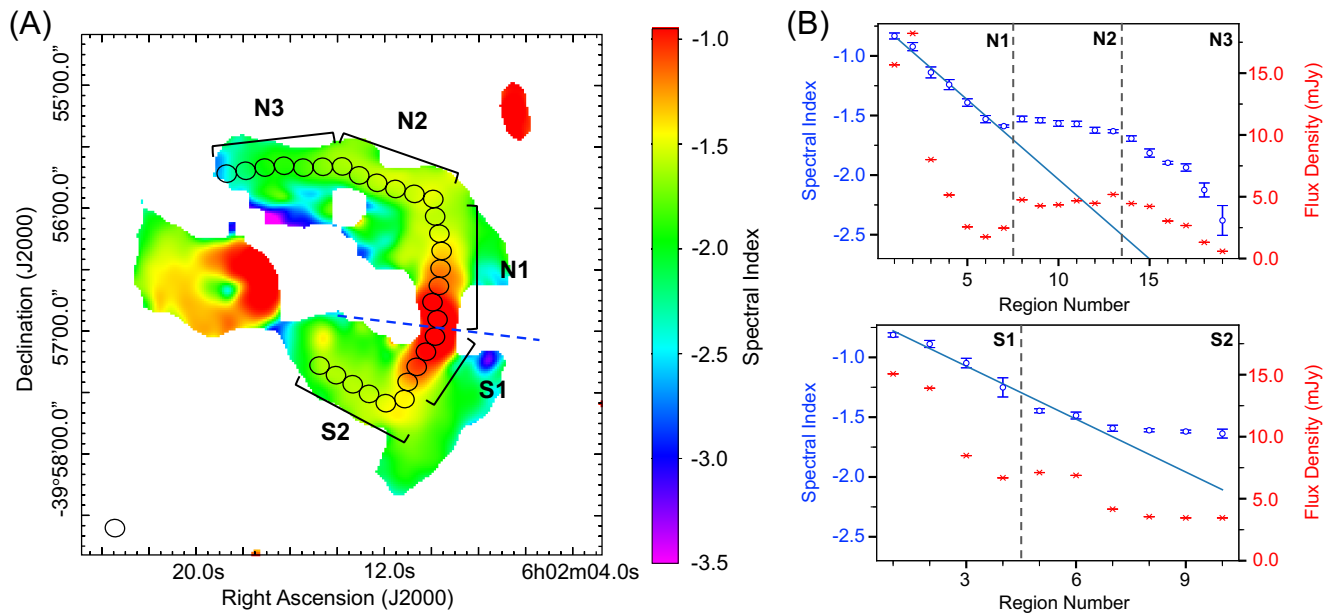


Figure 2. (A) Spectral index map derived from the radio datasets at 909-1658 MHz. Pixels with intensities below three times of total intensity rms levels are blanked. Black circles on MRC 0600-399 indicate the regions in which the spectral index and flux density values are calculated and shown in bottom plots. The ellipse at bottom-left corner is the image resolution of 9.50×8.50 arcsec². (B) Plots of spectral indices (blue) and flux densities (red) of the regions at the northern (top) and southern (bottom) jets. The horizontal axes show the region numbers. Each region 1 of the northern and southern jets is above and below the boundary line respectively, shown in the spectral index map with a blue-dashed line. The blue-solid lines are the results of linear fitting of spectral indices in N1 and S1.

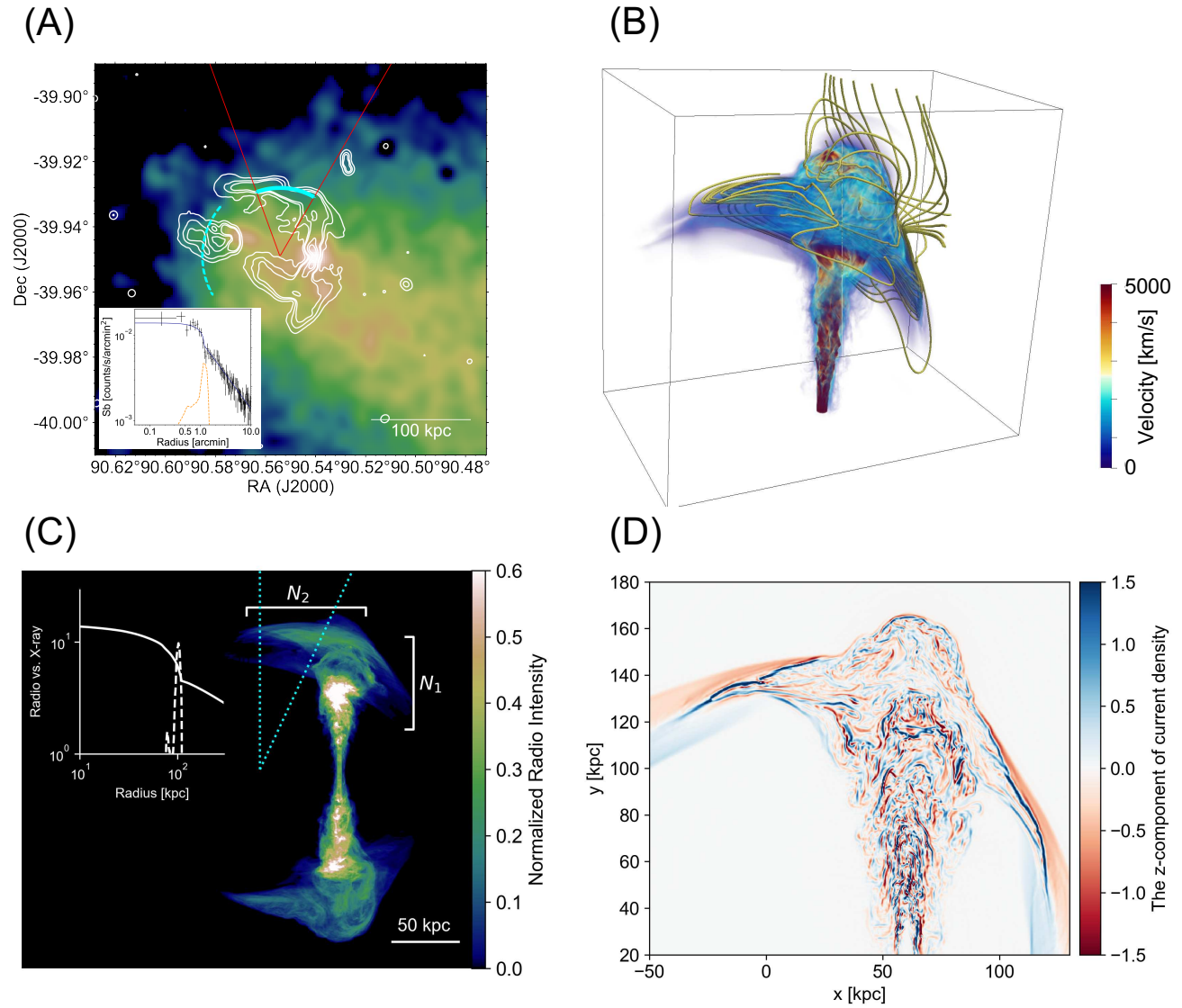


Figure 3. (A) XMM-Newton 0.5–2.0 keV band image with MeerKAT radio contours. The cyan arcs indicate the location of the cold front³. The solid cyan is this work. The red sector represent where the surface brightness was extracted. (A insert) Radial surface brightness profile of XMM-Newton data in 0.5–2.0 keV band across the northern bended radio emission. The blue solid and orange dashed lines represent the best-fit model of X-ray surface brightness profile and a radial profile of MeerKAT 1.28 GHz emission. At the peak of the radio emission ($r \sim 1.2'$), there is an indication of a dip in the X-ray radial profile which may suggest the presence of the strong magnetic pressure. (B) The 3D volume rendering of the absolute velocity for our MHD simulations at $t = 168$ Myr. Yellow lines show the variation of magnetic fields from initial fields, $\delta B = B(t = 168 \text{ Myr}) - B(t = 0)$. The box size is $234 \text{ kpc} \times 198 \text{ kpc} \times 126 \text{ kpc}$. (C) The projection plot shows the integrated synchrotron emissivity along a line of sight $\hat{n} = (0.06, 0.71, -0.64)$ at $t = 168$ Myr. The cyan sector represent where the surface brightness was extracted. (C insert) The white solid and dashed lines represent the X-ray surface brightness and the radio intensity profile. (D) The color map (sliced from 3D data at $z = 0$) shows the z-component of current density, $J_z = (\nabla \times B)_z$ at $t = 168$ Myr.

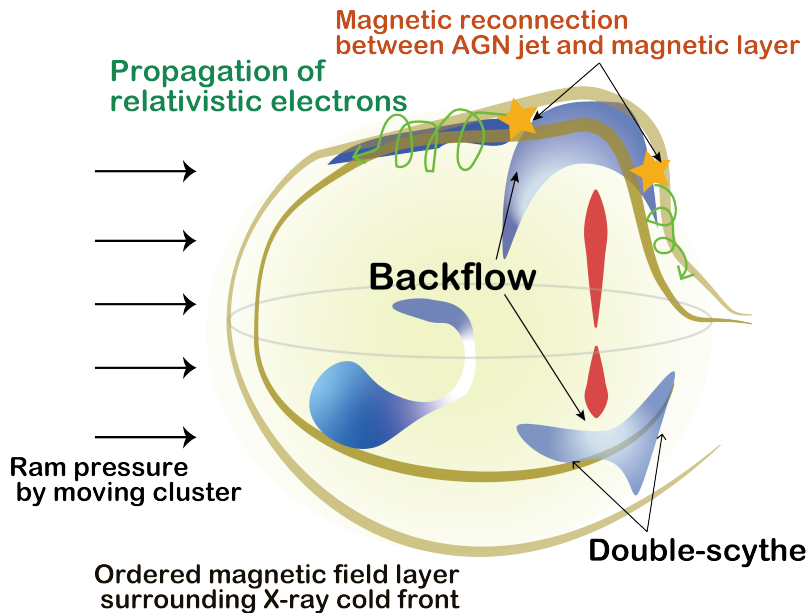


Figure 4. A schematic drawing to summarize of our findings both of the observations and numerical simulation. As a galaxy cluster moving within the hot plasma sweep the intercluster magnetic fields, the magnetic field compresses along the contact discontinuity, forming a magnetic layer. AGN jet ejected from the member galaxy of the cluster receives a ram pressure by proper motion. As MRC 0600-399 is the BCG, ram pressure does not work on their jets. When the jet terminal region reaches the magnetic layer on the cold front, the jet flow diverges along with the magnetic layer, called the “double-scythe” structure. Because the magnetic field in the AGN jet reconnects the magnetic layer, non-thermal particles accelerated by the magnetic reconnection propagate along with the magnetic layer. These particles emit synchrotron radiation. The north part of the jet locates on the rim of the cold front, while the south one hits it on the plan.

Figures

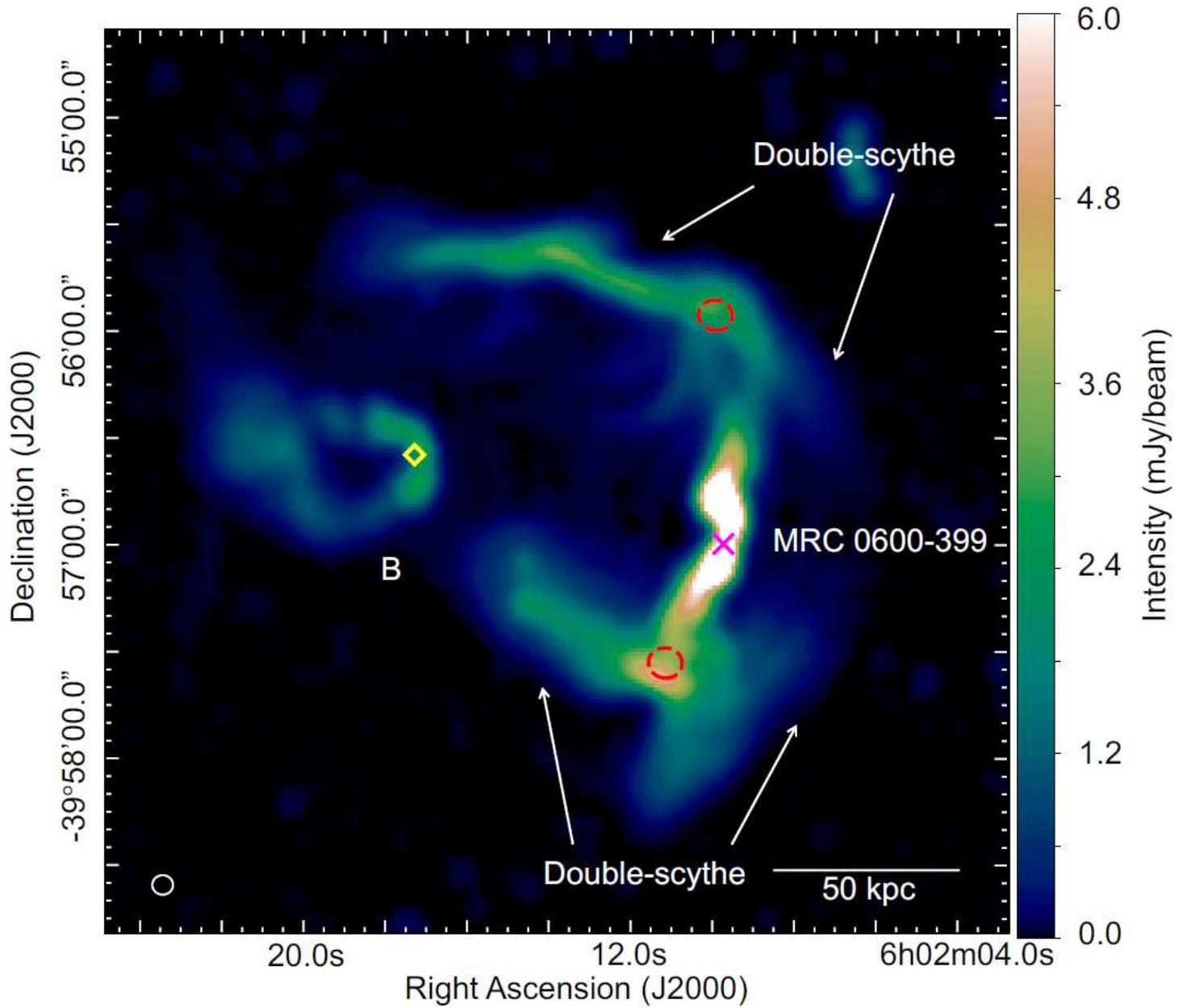


Figure 1

MeerKAT image of the total intensity at the center frequency of 1.28 GHz. The beam size is shown in bottom-left corner, 5.80×5.48 arcsec². The magenta cross point indicates the position of the 2nd brightest cluster galaxy in optical band associated with MRC 0600-399. MRC 0600-399 has jets which are bent 90 degree to the east, and continue to the east direction while keeping their collimated shapes. The arrows show the “double-scythe” structures, while the red dashed circles show the bend points. The yellow diamond point shows the position of optical source associated with galaxy B. Galaxy B has also a two-sided jet, but they bend gently and the southern jet has a plume-like structure at the tail. We determined the distance and the length of the scale bar on the basis of the values of the Hubble’s constant = $70 \text{ km s}^{-1} \text{ Mpc}^{-1}$ and the redshift $z=0.046$.

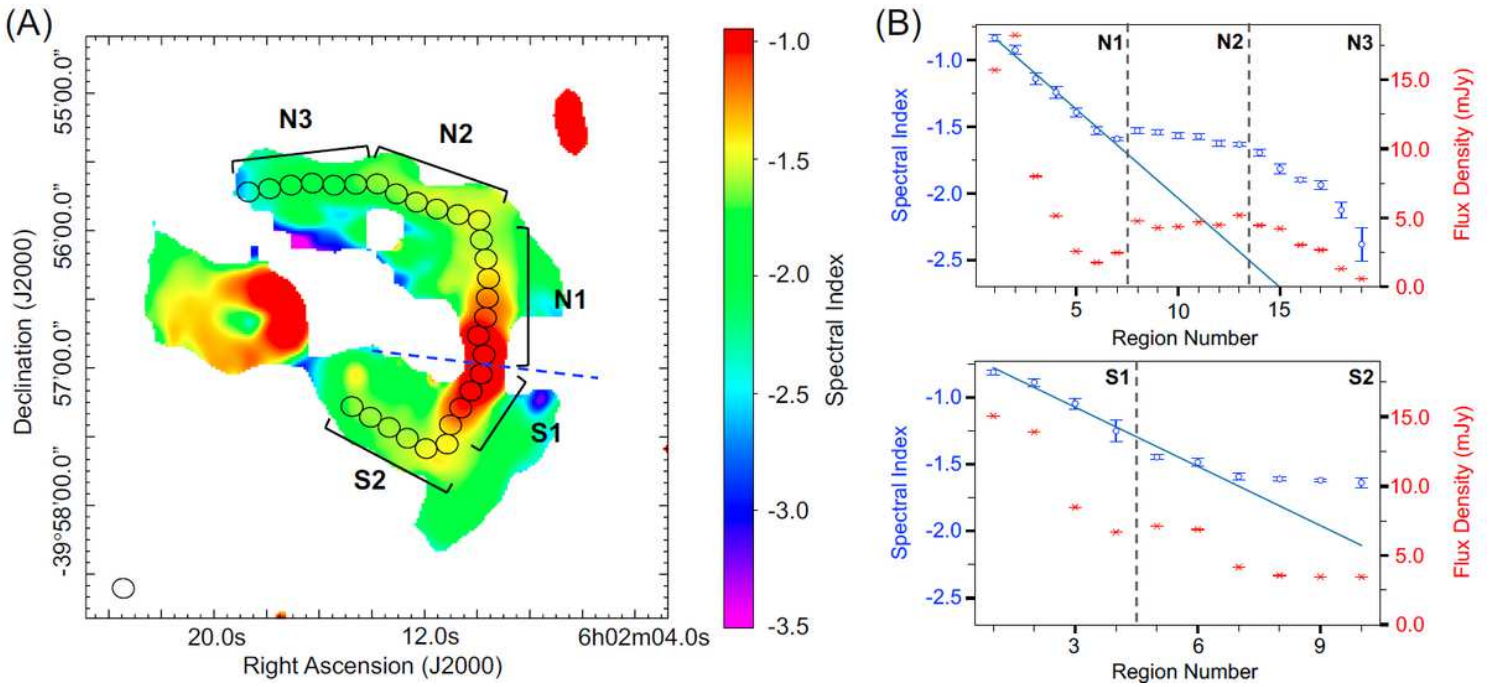


Figure 2

(A) Spectral index map derived from the radio datasets at 909-1658 MHz. Pixels with intensities below three times of total intensity rms levels are blanked. Black circles on MRC 0600-399 indicate the regions in which the spectral index and flux density values are calculated and shown in bottom plots. The ellipse at bottom-left corner is the image resolution of 9.50×8.50 arcsec². (B) Plots of spectral indices (blue) and flux densities (red) of the regions at the northern (top) and southern (bottom) jets. The horizontal axes show the region numbers. Each region 1 of the northern and southern jets is above and below the boundary line respectively, shown in the spectral index map with a blue-dashed line. The blue-solid lines are the results of linear fitting of spectral indices in N1 and S1.

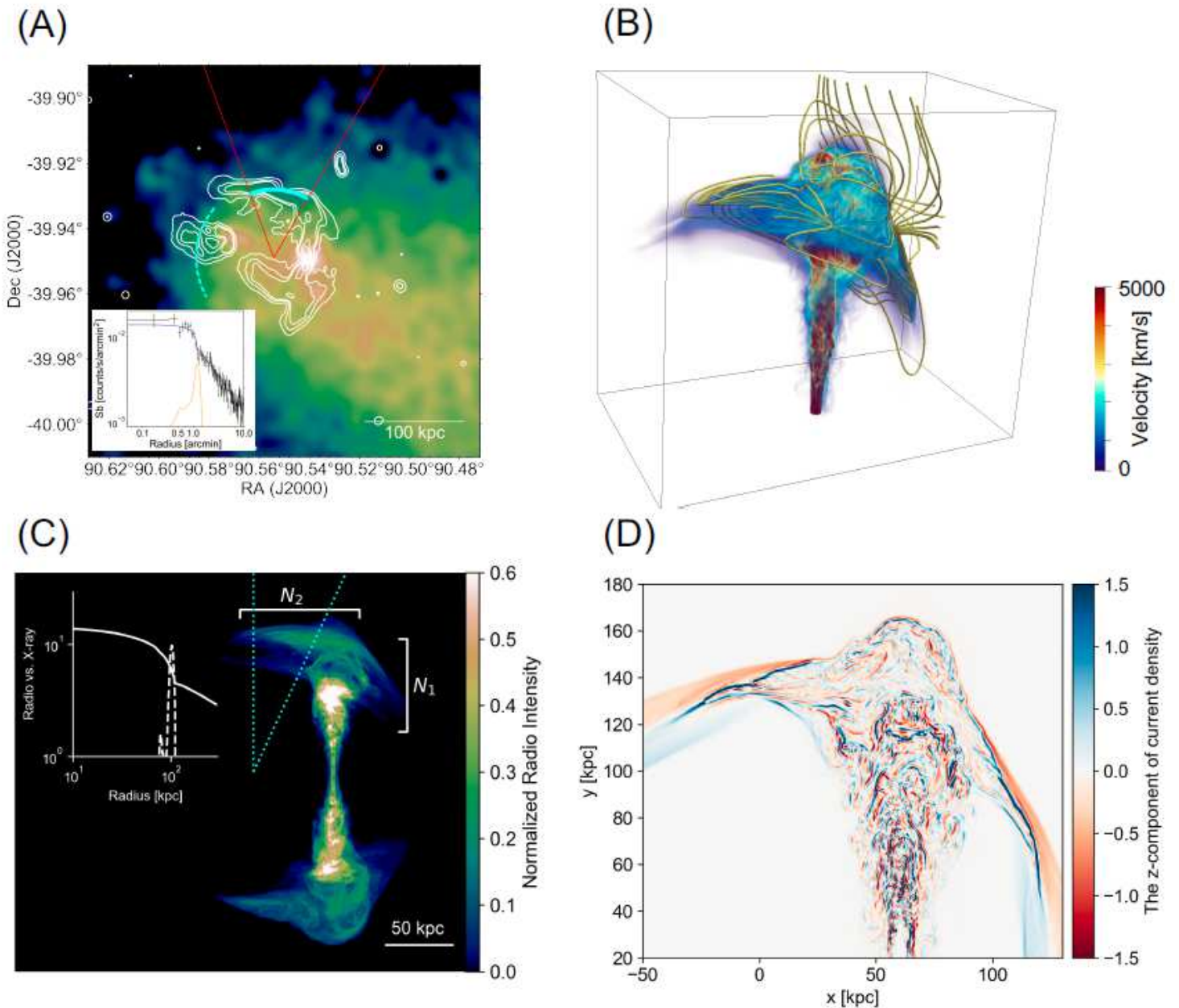


Figure 3

(A) XMM-Newton 0.5–2.0 keV band image with MeerkAT radio contours. The cyan arcs indicate the location of the cold front. The solid cyan is this work. The red sector represent where the surface brightness was extracted. (A insert) Radial surface brightness profile of XMM-Newton data in 0.5–2.0 keV band across the northern bended radio emission. The blue solid and orange dashed lines represent the best-fit model of X-ray surface brightness profile and a radial profile of MeerkAT 1.28 GHz emission. At the peak of the radio emission ($r \approx 1.2''$), there is an indication of a dip in the X-ray radial profile which may suggest the presence of the strong magnetic pressure. (B) The 3D volume rendering of the absolute velocity for our MHD simulations at $t = 168$ Myr. Yellow lines show the variation of magnetic fields from initial fields, $\delta B = B(t = 168 \text{ Myr}) - B(t = 0)$. The box size is $234 \text{ kpc} \times 198 \text{ kpc} \times 126 \text{ kpc}$. (C) The projection plot shows the integrated synchrotron emissivity along a line of sight $\hat{n} = (0.06, 0.71, -0.64)$ at $t = 168$ Myr. The cyan sector represent where the surface brightness was extracted. (C insert) The white

solid and dashed lines represent the X-ray surface brightness and the radio intensity profile. (D) The color map (sliced from 3D data at $z = 0$) shows the z-component of current density, $J_z = (\nabla \times \mathbf{B})_z$ at $t = 168$ Myr.

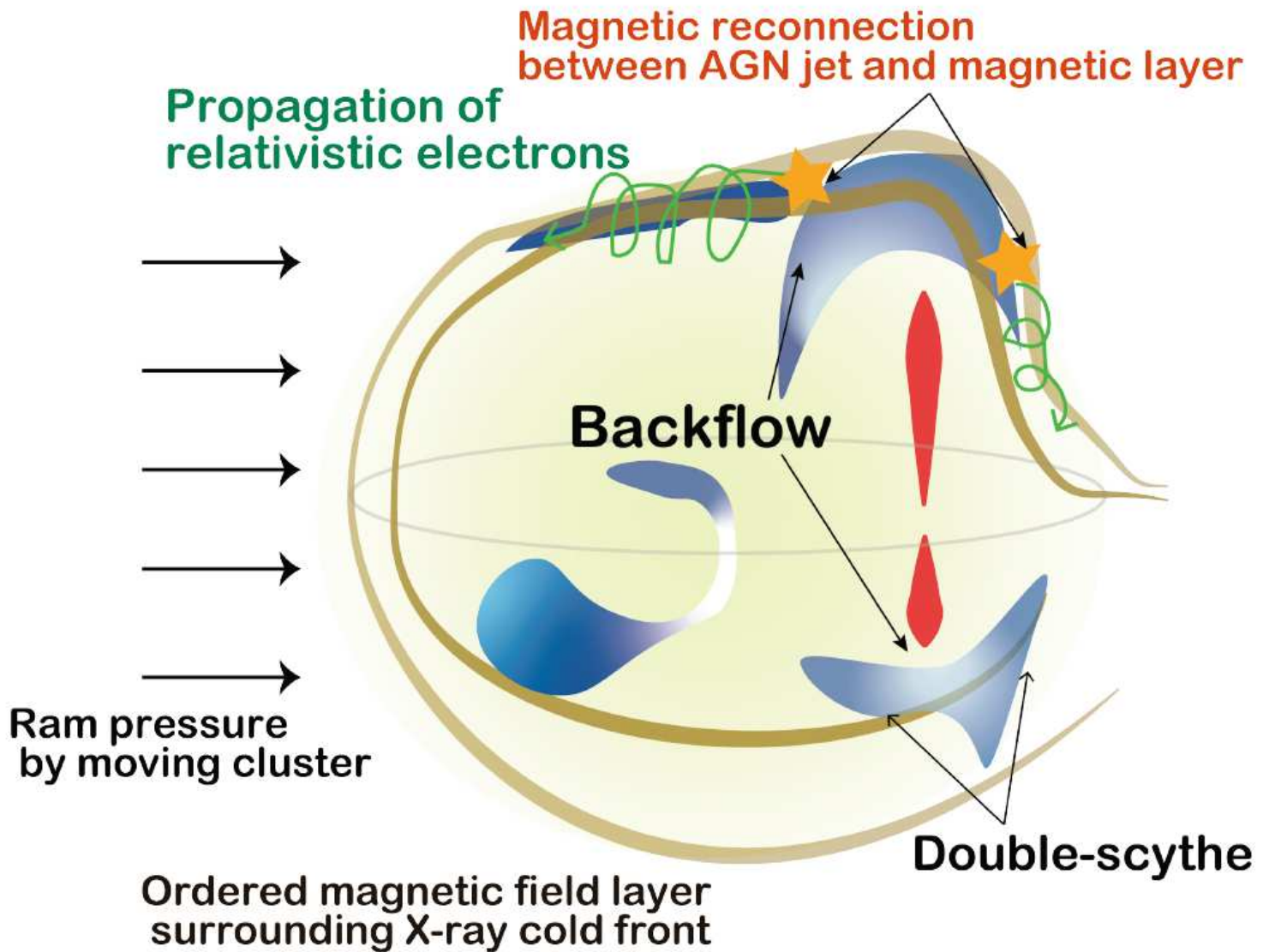


Figure 4

A schematic drawing to summarize of our findings both of the observations and numerical simulation. As a galaxy cluster moving within the hot plasma sweep the intercluster magnetic fields, the magnetic field compresses along the contact discontinuity, forming a magnetic layer. AGN jet ejected from the member galaxy of the cluster receives a ram pressure by proper motion. As MRC 0600-399 is the BCG, ram pressure does not work on their jets. When the jet terminal region reaches the magnetic layer on the cold front, the jet flow diverges along with the magnetic layer, called the “double-scythe” structure. Because the magnetic field in the AGN jet reconnects the magnetic layer, non-thermal particles accelerated by the magnetic reconnection propagate along with the magnetic layer. These particles emit synchrotron radiation. The north part of the jet locates on the rim of the cold front, while the south one hits it on the plan.